Heterostructuring Mesoporous 2D Iridium Nanosheets with Amorphous Nickel Boron Oxide Layers to Improve Electrolytic Water Splitting

Yunqing Kang, Bo Jiang, Victor Malgras, Yanna Guo, Ovidiu Cretu, Koji Kimoto, Aditya Ashok, Zhe Wan, Hexing Li, Yoshiyuki Sugahara, et al.

Heterostructuring Mesoporous 2D Iridium Nanosheets with Amorphous Nickel Boron Oxide Layers to Improve Electrolytic Water Splitting

Yunqing Kang,[1,2] Bo Jiang,*[4] Victor Malgras,*[2] Yanna Guo,[1] Ovidiu Cretu,[3] Koji Kimoto,[3] Aditya Ashok,[6] Zhe Wan,[4] Hexing Li,[4] Yoshiyuki Sugahara,[1,5] Yusuke Yamauchi[2,5,6] and Toru Asahi*[1,5]

1 Department of Nanoscience and Nanoengineering, Department of Life Science and Medical Bioscience, and Department of Applied Chemistry, Faculty of Science and Engineering, Waseda University, 3-4-1 Okubo, Shinjuku, Tokyo 169-8555, Japan

2 JST-ERATO Yamauchi Materials Space-Tectonics Project and International Center for Materials Nanoarchitectonics (WPI-MANA), National Institute for Materials Science (NIMS), 1-1 Namiki, Tsukuba, Ibaraki 305-0044, Japan

3 Electron Microscopy Group, National Institute for Materials Science (NIMS), 1-1 Namikie, Tsukuba, Ibaraki 305-0044, Japan

4 The Education Ministry Key Lab of Resource Chemistry and Shanghai Key Laboratory of Rare Earth Functional Materials, Shanghai Normal University, Shanghai 200234, China

5 JST-ERATO Yamauchi Materials Space-Tectonics Project, Kagami Memorial Research Institute for Materials Science and Technology, Waseda University, 2-8-26 Nishiwaseda, Shinjuku, Tokyo 169-0051, Japan

6 Australian Institute for Bioengineering and Nanotechnology (AIBN) and School of Chemical Engineering, The University of Queensland, Brisbane, QLD 4072, Australia

Abstract

Two-dimensional (2D) heterostructures exhibit a considerable potential in electrolytic water splitting due to their high specific surface areas, tunable electronic properties, and diverse hybrid compositions. However, the fabrication of well-defined 2D mesoporous amorphous-crystalline heterostructures with highly active heterointerfaces remains challenging. Herein, an efficient 2D heterostructures comprised of amorphous nickel boron oxide (Ni-B_i) and crystalline mesoporous iridium (meso-Ir) is designed for water splitting, referred to as Ni-B_i/meso-Ir. Benefiting from well-defined 2D heterostructures and strong interfacial coupling, the resulting mesoporous dual-phase Ni-B_i/meso-Ir heterostructures possess abundant catalytically active heterointerfaces and boost the exposure of active sites, compared to their crystalline and amorphous mono-counterparts. The electronic state of iridium sites has been tuned favorably by coordinating with Ni-B_i layers. Consequently, the Ni-B_i/meso-Ir heterostructures show superior electrochemical performance towards both oxygen evolution reaction (OER) and hydrogen evolution reaction (HER) in an alkaline electrolyte with fabulous stability.

Keywords: *Mesoporous materials; 2D materials; heterostructures; amorphous-crystalline interfaces; water splitting.*

Introduction

Electrochemical water splitting for hydrogen and oxygen production is considered as one of the most promising strategies to harvest solar and wind energy.[1,2] However, the sluggish kinetics of the two water electrolysis half-reactions, composed of the hydrogen evolution reaction (HER) at the cathode and oxygen evolution reaction (OER) at the anode, hamper the scalable industrial application.[3] It is of great significance to develop highly efficient HER and OER bifunctional electrocatalysts in the same electrolyte to simplify the device fabrication.[4,5] One effective strategy to develop highly effective water splitting electrocatalysts is based on heterostructure engineering due to their high specific surface areas and the synergistic effects among different components.[6,7] Specially, the heterostructures utilizing two-dimensional (2D) materials always possess rich active sites, short mass/charge transport distances, and unique face-contact heterointerfaces which have large interface areas and special electronic structures. These features can not only preserve the intrinsic catalytic activities of each component, but also are beneficial to increase catalytic performances because of the interfacial synergistic effects between the different components.[8−13] Unfortunately, most of the previous reported 2D heterostructures materials mainly based on traditional 2D layered materials as host materials, such as graphene, metal sulfides/nitrides, or C_3N_4 without any porous architectures.[14−16] There is still rarely reported on well-defined 2D metallic-based heterostructures by a simple chemical reduction method because of the weak interaction between different metal components and difficult kinetic growth control. In addition, previous reported 2D layered heterostructures are randomly assembly lacking intimate and efficient coupling, which devalues the function of heterostructures. Therefore, synthesis of 2D metal heterostructures consisting of oriented growth manner between heterostructures remains a great challenge and bring a new generation of electrocatalysts for maximizing the performance.

2D iridium (Ir) structures have been reported as the most efficient and important cathodic electrocatalysts towards water splitting in both acidic and alkaline electrolytes.[17−19] Cost is a central concern in industrial-scale catalysis; thus, hybridizing Ir with other Earth-abundant elements-based nanomaterials can reduce the content of Ir and improve its catalytic performance *via* taking advantage from the synergy between the different components.[20−23] However, the reports based on heterostructure engineering only focused on the loading of Ir nanoparticles/cluster on traditional 2D materials (*e.g.*, metal hydroxides and graphene), which lacks large contacted heterointerfaces.[24−27] Our previous reports have successfully constructed 2D Ir with mesoporous networks which shows excellent OER activity under acidic media due to rich defect sites and larger specific surface area.[28] Nevertheless, the construction of non-noble metal-based

materials with mesoporous Ir nanosheets forming a 2D heterostructure and the consequent effect of the resultant catalyst on both OER and HER performance in alkaline electrolytes have never been explored.

Except for controlling the composition and morphology of 2D Ir materials, recently phase engineering *via* amorphous-crystalline heterostructures has attracted a lot of attention in catalytic applications owing to their intriguing phase-dependent properties.[29–31] Due to its unique short-range ordered and long-range disordered atomic arrangement, amorphous phases have a greater proportion of coordinatively unsaturated sites, facilitating the ion diffusion and adsorption of reactants.[32–34] In addition, the flexibility of the local structure in amorphous phases can accelerate charge transfer between active sites and intermediates. Metal-boron amorphous materials, in particular, are most promising catalysts in extensive applications, including petrochemical production, energy conversion and environmental catalysis.[35] However, the low conductivity of amorphous phase limits its electrocatalytic applications.[36] To overcome this shortcoming, integrating amorphous materials with crystalline metal to obtain amorphous-crystalline heterostructures is proved to be a very efficient way to harmonize the individual advantages of amorphous and crystalline phases, thereby promote activity and stability.[31,37] Nevertheless, it is difficult to construct such kind of heterointerfaces between the crystalline metal and the amorphous metal-boron because the covalent component in metal-metalloid bonds is intrinsically different from its crystalline counterparts.[34] It is, therefore, necessary not only to develop high-performance 2D heterostructured electrocatalysts combining crystalline mesoporous Ir nanosheets and amorphous metal-boron-based materials, but also to investigate the synergy taking place between them to enhance electrocatalytic activity.

In this study, we develop a facile *in-situ* growth method to prepare 2D heterostructures of amorphous nickel-boron oxide (Ni-B_i) layers coupling with crystalline mesoporous iridium (meso-Ir) by a two-step wet-chemical reduction strategy. The Ni-B_i layers represent a new breed of low-cost material and display higher catalytic performance than their counterparts such as metal oxides.[38] In this study, the as-prepared 2D mesoporous heterostructures both maximize the exposed active sites to take part in the reaction and possess rich amorphous-crystalline heterointerfaces. Thus, the obtained Ni-B_i/meso-Ir catalyst shows excellent activity and stability for both OER and HER under alkaline condition. The enhanced water splitting performance can be mainly ascribed to the abundant active sites and the synergistic effects, electronic interaction, and coordination effects between the Ir and Ni-B_i at the heterostructured interfaces. This study provides a useful approach to the rational design of porous metal-based 2D heterostructures and helps us better understand the role of the dual-phase interfaces.

Results and discussion

The dual-phase 2D Ni-B_i/meso-Ir heterostructures with amorphous nickel boron oxide layers anchored on the pore surface of mesoporous Ir nanosheets were successfully synthesized by a two-step wet-chemical reduction method. Similarly to a previously reported method,[28] the meso-Ir nanosheets are first templated with polystyrene-poly(ethylene oxide) (PS-*b*-PEO) block copolymer micelles, using formic acid as a reducing agent (see the SEM image in **Figure 1a**). The gradual reduction process from Ir^{4+} to Ir^0 can be clearly visualized through the photographs of the reaction vials in **Figure S1**. The obtained meso-Ir nanosheets mixed with a Ni^{2+} aqueous solution are dispersed in water and kept under stirring for 30 min, cooled in an ice bath, followed by the injection of an ice-cool sodium borohydride solution (SBH). After stirring for another 60 min, the product is repeatedly washed with ethanol and separated through centrifugation. The final Ni-B_i/meso-Ir catalyst is then dried at room temperature and annealed at 150 °C for 30 min under N_2 atmosphere to remove any impurities. **Figures 1b** and **1c** show the scanning electron microscopy (SEM) and transmission electron microscopy (TEM) images of the Ni-B_i/meso-Ir heterostructures, respectively, where the mesoporous Ir nanosheets appear to be uniformly covered with Ni-B_i layers, which could also be seen at low-magnification SEM and TEM images (**Figure S2**). Furthermore, the superior hydrophilicity of Ni-B_i/meso-Ir compared to bare meso-Ir indicates that it is a more suitable environment for the adsorption of reactants and diffusion of electrolyte (inset of **Figures S2a** and **S2c**).[39] The final molar ratio of Ir, Ni, and B in Ni-B_i/meso-Ir heterostructures was determined from inductively coupled plasma optical emission spectroscopy (ICP-OES) to be 46.7:44.3:9.0.

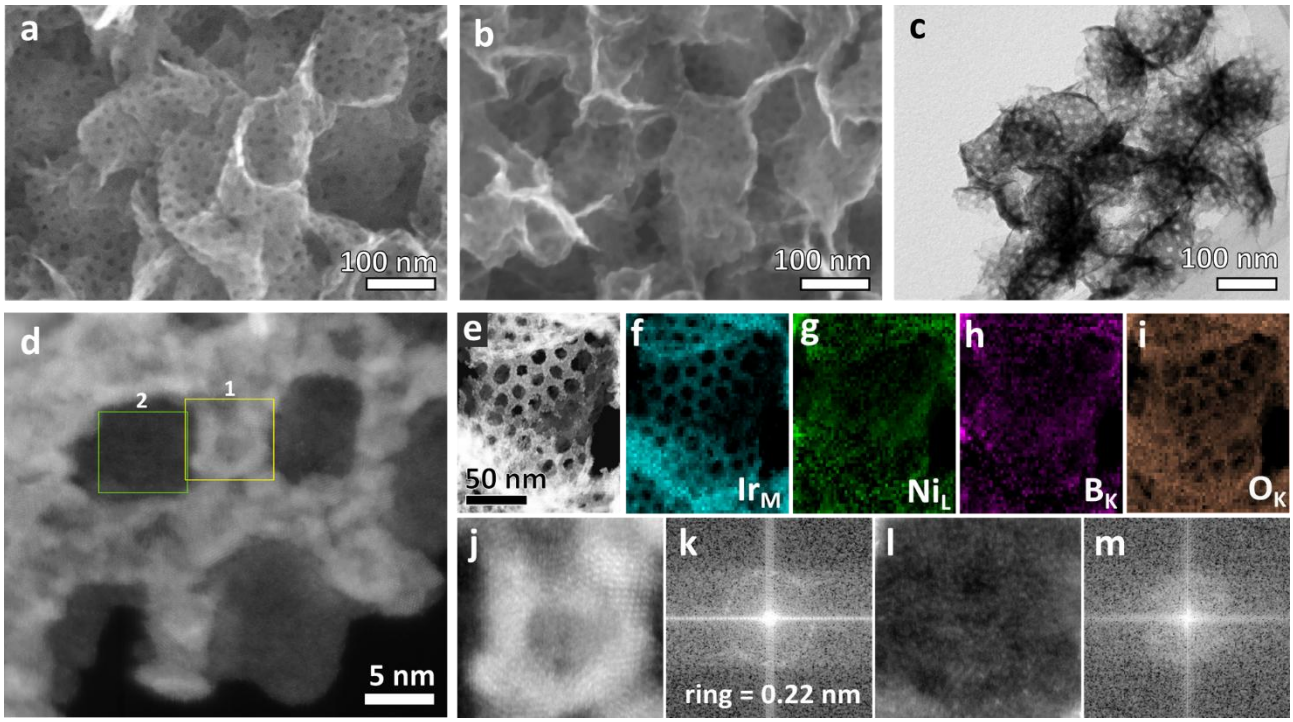

Figure 1. SEM images of (a) bare meso-Ir nanosheets and (b) nickel boron oxide/meso-Ir (Ni-B_i/meso-Ir) heterostructures. (c) TEM and (d) high-magnification HAADF-STEM images of Ni-B_i/meso-Ir heterostructures. (e) Lower-magnification HAADF-STEM image of a different part of the Ni-B_i/meso-Ir heterostructures. (f-i) EELS signal maps for the area in (e) corresponding to the Ir-M, Ni-L, B-K and O-K edges, respectively. (j, k) Enlarged image and corresponding FFT from area "1" of (d); a ring of spots corresponding to a lattice spacing of 0.22 nm is visible. (l, m) Enlarged image and corresponding fast Fourier transform (FFT) from area "2" of (d).

To investigate the detailed structural information of dual-phase Ni-B_i/meso-Ir heterostructures, high-resolution high-angle annular dark-field scanning transmission electron microscopy (HAADF-STEM) measurements were conducted. As shown in **Figure 1d**, the numerous Ir nanocrystalline domains (bright contrast) can be observed in the pore wall of the nanosheets, while the darker contrast suggests the presence of a thin layer covering both the Ir matrix and the pores. Elemental mapping of the sample performed using electron energy-loss spectroscopy (EELS, **Figures 1e-i**) confirm that the Ir, Ni, B and O are homogeneously distributed. These images clearly show that Ir follows the mesoporous pattern, while Ni and B are homogeneously distributed over the surface. The high-resolution images in **Figure 1j** and **1l** also highlight the crystalline nature of the Ir skeleton, with a lattice spacing of 0.22 nm corresponding to the (111) plane of the face-centered cubic (*fcc*) structure (**Figure 1k**), while the Ni-B_i layers covering the pores remains amorphous (**Figure 1m**). The coupled heterointerface could also be confirmed by HRTEM analysis (**Figure S3**). The amorphous-crystalline interface has been previously reported to be expected to facilitate the adsorption of reaction intermediates and enhance catalytic activity.[40] In addition, the dual-phase structure of the as-prepared Ni-B_i/meso-Ir heterostructures was further studied by wide-angle X-ray diffraction (XRD) (**Figure 2a**). The diffraction pattern of the meso-Ir nanosheets shows four major peaks, assigned to typical (111), (200), (220) and (311) facets of the *fcc* Ir phase (JCPDS No: 06–0598). After coupling with Ni-B_i layers, no additional diffraction peaks were detected, further confirming the amorphous nature of Ni-B_i. Different from noble-metal-metalloid (*eg.* Pd-B) nanomaterials that form crystalline phase [41−43], the introduction of B into the non-noble metals such as Ni and Co during the chemical reduction process using strong reducing agents including sodium borohydride or dimethylamine borane usually cause long-range disordered structure.[44,45] This is supported by the XRD patterns of the bare Ni-B nanoparticles (NPs) before and after thermal treatment (**Figure S4**), exhibiting one single broad diffraction peak at around 2θ = 45°. The small-angle X-ray scattering (SAXS) was used to determine the periodicity of the mesoporous structure of Ni-B_i/meso-Ir and confirm that the structure observed by TEM is representative of the entire sample. As

shown in **Figure 2b**, a single diffraction peak of meso-Ir located at q = 0.26 nm^{-1} (d = 24 nm) shows the periodic mesoporous structure. The slight decrease in peak intensity of Ni-B$_i$/meso-Ir heterostructures in SAXS indicates the successful hybridization of the flexible Ni-B$_i$ layers in the pores of the meso-Ir nanosheets. Nitrogen (N_2) adsorption–desorption isotherm measurements (**Figure 2c**) exhibit typical type IV isotherms for both the meso-Ir and Ni-B$_i$/meso-Ir heterostructures; however, the Brunauer–Emmett–Teller (BET) surface area of Ni-B$_i$/meso-Ir heterostructure is smaller than for bare meso-Ir. According to the Barrett–Joyner–Halenda (BJH) method, the average pore size of Ni-B$_i$/meso-Ir (~11.5 nm) is smaller than that of meso-Ir (~13.3 nm) (**Figure S5**). These results indicate that part of Ni-B$_i$ layers is successfully loaded inside the pores of meso-Ir.

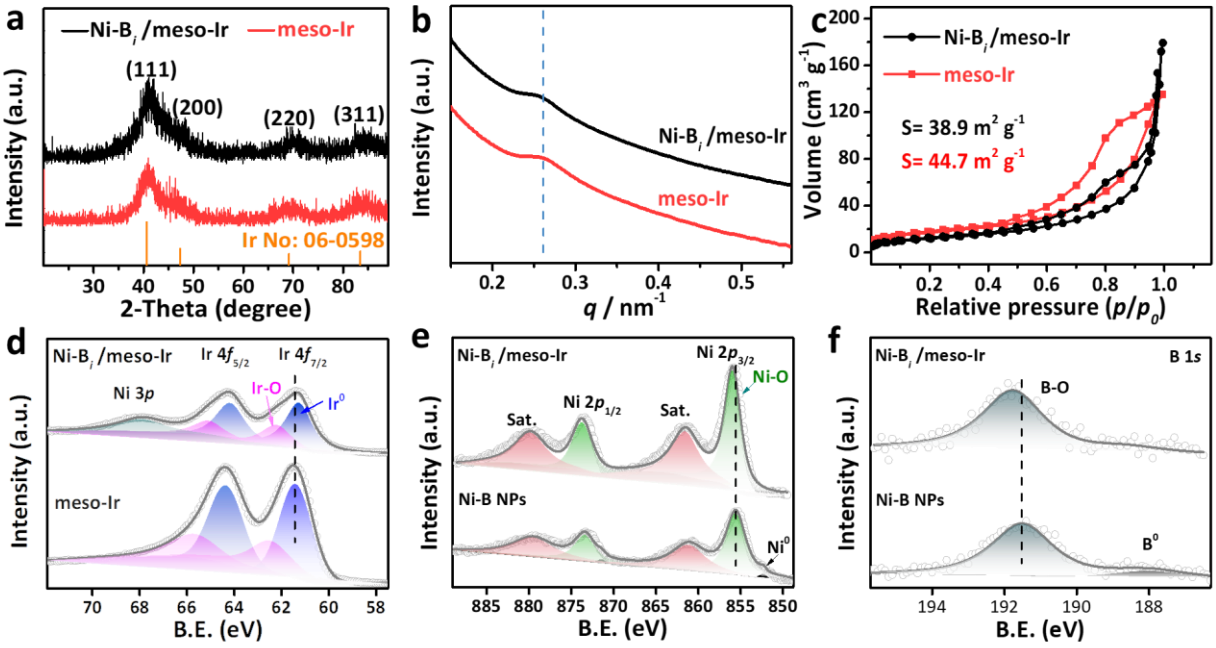

Figure 2. (a) XRD patterns, (b) SAXS patterns, and (c) the N_2 adsorption−desorption isotherm of bare meso-Ir and Ni-B$_i$/meso-Ir heterostructures. X-ray photoelectron spectroscopy of different samples resolved around d) Ir 4f, (e) Ni 2p and (f) B 1s.

X-ray photoelectron spectroscopy (XPS) was performed to identify the electronic structure of Ni-B$_i$/meso-Ir heterostructure. The Ir 4*f*, Ni 2*p*, O 1*s*, and B 1*s* core level XPS spectra of the Ni-B$_i$/meso-Ir sample confirm the presence of Ir, Ni, B, and O elements. As shown in **Figure 2d**, the Ir 4*f* peaks in Ni-B$_i$/meso-Ir heterostructures shifts towards lower binding energies compared with bare meso-Ir. The Ni^0 and B^0 peak at 852.3 and 188.0 eV could be observed in bare Ni-B NPs, respectively; however, the Ni and B in Ni-B$_i$/meso-Ir heterostructures exist mainly in a highly oxidized Ni-O (Ni^{2+} and Ni^{3+}) state,[46] likely

resulting from that the ultrathin layers structure is more spontaneous oxidation in air and the electron transfer between Ni-B_i and meso-Ir (**Figure S2e,f**). A high-resolution XPS spectrum of O 1s (**Figure S6**) can be divided into O1, O2, and O3 species, which are assigned to lattice oxygen, substituted hydroxyl group and adsorbed oxygen, respectively.[47] Moreover, the binding energies of Ni 2*p* and B 1*s* in Ni-B_i/meso-Ir heterostructure both exhibit a positive shift with respect to the bare Ni-B NPs. These findings suggest strong electronic interaction between meso-Ir and Ni-B_i layers and facilitated charge transfer at the interface. Previous reports have suggested that such property can be beneficial to tune the electronic structure local to the surface and reduce the free energy of adsorption of undesired intermediates, thus improving catalytic activity.[48–50]

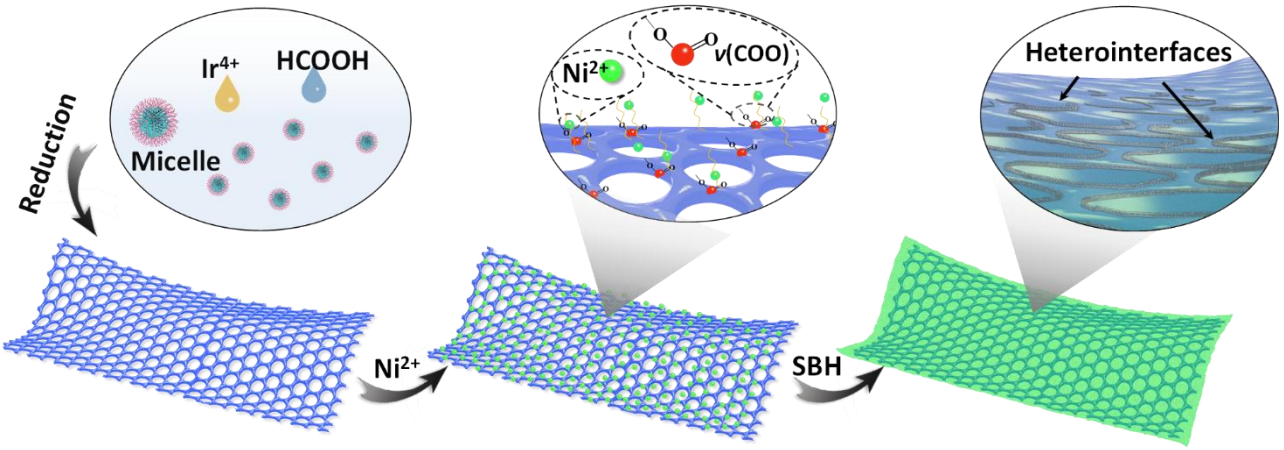

Figure 3. Schematic illustration of the synthesis of Ni-B_i/meso-Ir heterostructures.

To better understand the formation process of 2D heterostructures, we analyzed the growth mechanism of nickel boron oxide on meso-Ir surface, as illustrated in **Figure 3**. To prepare bare meso-Ir nanosheets, formic acid acts both as a reducing agent and 2D structure-directing agent. As it self-decomposes into carbon monoxide (CO) during the reduction process, CO binds to the (111) facet of Ir nanocrystals to facilitate the growth of nanosheets.[51,52] The presence of CO on the surface of the Ir metal can be detected by Fourier transform infrared spectroscopy (FTIR), which shows a typically absorption band at ~2062 cm^{-1} (**Figure S7a**).[53] These CO molecules are still present after coating with amorphous Ni-B_i, but disappear after thermal treatment at 150 °C (**Figure S7a**). In addition, the symmetric stretching modes of carboxylic group *ν*(COO) is also observed at absorption band between 1320 and 1400 cm^{-1} in FTIR, indicating that some formic acid molecules remain adsorbed on the metal surface during chemical reduction process (**Figure S7b**).[54,55] Notably, the peak intensity of *ν*(COO) in FTIR is significantly reduced after hybridization with amorphous Ni-B_i layers prior to the thermal treatment (**Figure S7b**). This can be

expected as carboxylic groups participate to the effective adsorption of metal ions (*i.e.* Ni^{2+}).[56,57] Moreover, 2D Ir mesoporous nanosheets provide a platform for the growth of Ni-B_i layers. Specifically, pre-adsorbed Ni^{2+} ions on the surface of Ir nanosheets are first reduced into ''Ni-B seeds'', where Ni-B_i later grow along the plane, resulting in a coating-layer structure. **Figure S8** shows how the amount of Ni precursor affects the formation of the ultrathin Ni-B_i layers. The maximum Ni precursor concentration before triggering the formation of visible particles (**Figure S8e,f**) is considered optimal. For additional insights, SEM images of bare amorphous Ni-B nanoparticles (NPs) obtained without the support of meso-Ir, nonporous Ir prepared without a PS-*b*-PEO porogen, as well as Ni-B/nonporous Ir heterostructures are presented in **Figures S9a**, **b** and **c**, respectively. These finding confirmed the rationality of the proposed growth mechanism of 2D heterostructures. The method can also be extended to prepare Co-B_i/meso-Ir heterostructures, as shown in **Figure S10**.

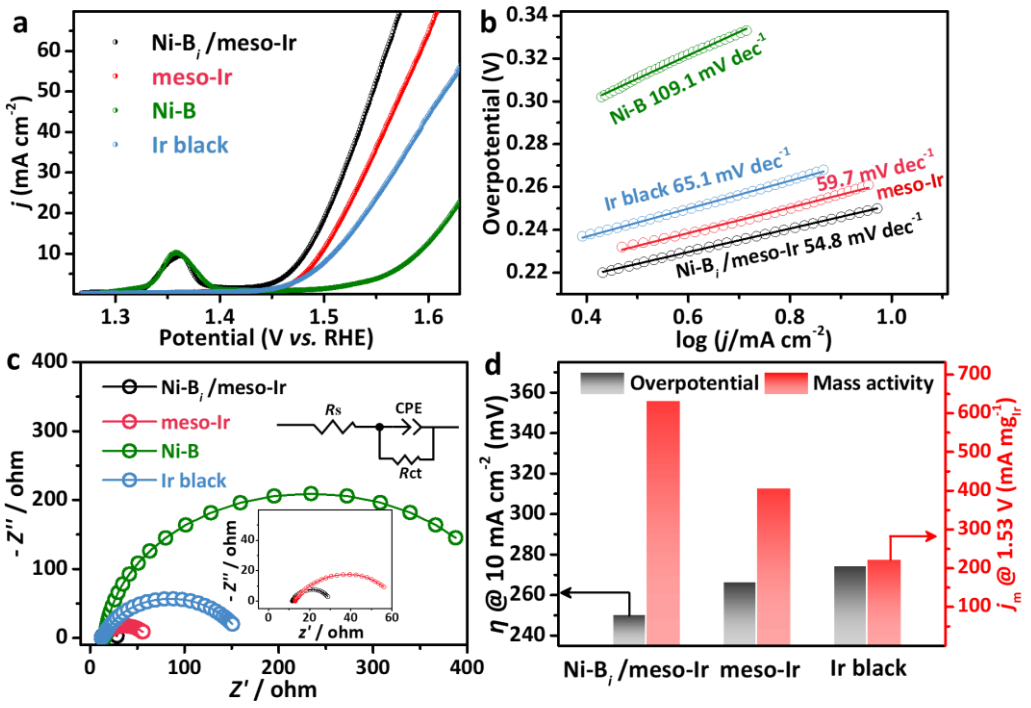

Figure 4. (a) OER polarization curves, along with the corresponding (b) Tafel plots of Ni-B_i/meso-Ir, meso-Ir, Ni-B, and commercial Ir black. (c) EIS analyses Nyquist plots of the different catalysts performed at 1.48 V *vs.* RHE (inset shows the enlarged EIS plots of Ni-B_i/meso-Ir and meso-Ir, and the equivalent circuit model). (d) Comparison of overpotential (η) to drive a current density of 10 mA cm^{-2} and mass activity (j_m) at 1.53 V (*vs*. RHE). All catalysts were examined using 1.0 M KOH as the electrolyte at the scan rate of 10 mV s^{-1} and corrected by *iR* compensation.

Inspired by the unique 2D mesoporous morphology and rich heterointerface of the dual-phase, we evaluated the electrocatalytic performances of Ni-B_i/meso-Ir for both OER and HER in a 1.0 M KOH solution using a three-electrode system. The working electrode was obtained by mixing the as-prepared Ni-B_i/meso-Ir and carbon black (Vulcan XC–72) and annealing the mixture in an N_2 atmosphere at 150 °C for 30 min. Bare meso-Ir and Ni-B NPs were also prepared with a similar procedure. As observed from the linear sweep voltammetry (LSV) curves in **Figure 4a**, the Ni-B_i/meso-Ir shows superior OER activity compared to the bare meso-Ir and Ni-B NPs. Both Ni-B_i/meso-Ir and Ni-B NPs show a typical redox peak at 1.36 V because of the transition from Ni^{2+} to Ni^{3+},[58] which is known to improve OER activity in an alkaline electrolyte.[59] Under the same reaction conditions, a smaller overpotential of 250 mV yielding 10 mA cm^{-2} is required for Ni-B_i/meso-Ir, which is lower than those of the meso-Ir (266 mV), Ni-B NPs (358 mV), and commercial Ir black (278 mV). It has been proposed that the double-layer capacitance (C_{dl}) of the sample in the non-Faraday region can reflect its electrochemical active surface area (ECSA).[60] Our study (**Figure S11a-c**) shows a larger C_{dl} of the Ni-B_i/meso-Ir (31.4mF cm^{-2}) compared with meso-Ir (25.9 mF cm^{-2}), and the ECSA-normalized OER LSV curves indicate that the heterostructured sample yield a slightly higher current density (**Figure S11d**). These results suggest that the superior activity observed in **Figure 4a** can partly be imputed to additional active sites inherent from the Ni-B_i layer. To obtain deeper insight into the enhanced OER activity, the corresponding Tafel plots were recorded to assess the underlying reaction kinetics (**Figure 4c**). A Tafel slope of 54.8 mV dec^{-1} is measured for Ni-B_i/meso-Ir, which is much lower than those of meso-Ir (59.7 mV dec^{-1}), Ni-B NPs (109.1 mV dec^{-1}), and Ir black (65.1 mV dec^{-1}), suggesting more efficient OER kinetics of Ni-B_i/meso-Ir.[61] Furthermore, the charge transfer kinetics was investigated by electrochemical impedance spectroscopy (EIS). The results in **Figure 4d** show that Ni-B_i/meso-Ir possesses the smallest semicircle in the low-frequency range, suggesting a lower charge transfer resistance (R_{ct}). This is an indication that coupling meso-Ir with Ni-B_i layers could promote electron conductivity, contributing to the superior OER catalytic activity. Moreover, the much smaller contact angle (inset **Figures S2a** and **c**) observed for Ni-B_i/meso-Ir (59°) compared that of meso-Ir (71°) indicates that the Ni-B_i layer increases hydrophilicity, which can then improve the adsorption of reactants (*ie*. H_2O or OH^-) and promote electrolyte diffusion. Additionally, when the activities of the samples are normalized to the noble metal iridium loading, the mass activity of Ni-B/meso-Ir for OER at 1.53 V(*vs*. RHE) is 630.5 mA mg^{-1}_{Ir}, which is 1.6 and 2.9 times greater than those of the meso-Ir and Ir black, respectively (**Figure 4d**). The above results indicate that the heterostructure constructed from Ni-B_i/meso-Ir heterostructures coupled with Ni-B_i layers coupling with 2D meso-Ir nanosheets possesses rich dual-phase interfaces, both in terms of ECSA and charge transfer, thus promoting the catalytic performance.

To confirm the unique structural advantage assigned to Ni-B_i/meso-Ir, we compared its OER activity with other composites where Ni-B formed a coarse heterointerface (see Experimental Section in the Supporting Information), or where nonporous Ir was used. One is to thermally treat the as-prepared meso-Ir (t-meso-Ir), and then deposited amorphous Ni-B NPs on its surface, forming a Ni-B/t-meso-Ir composites (**Figure S9d**). Another is physical mixed sample obtained by mixing the Ni-B NPs and meso-Ir (**Figure S9e**). The inferior OER activities of these samples (**Figure S9f**) highlight the importance of close interactions at the heterointerfaces between the amorphous nickel boron oxide layers and the 2D crystalline meso-Ir nanosheets by the *in situ* strategy, enabling faster mass/electron transfer and strong dual-phase synergy. Moreover, using non-porous Ir also resulted in inferior performance, evidencing the necessity of short pathways for mass diffusion and high active area, promoted by the 2D mesoporous structure. We also synthesized 2D mesoporous $Ni(OH)_2$/meso-Ir (**Figure S12a-c)** to understand the importance of the presence of B in the catalyst. The resulting lower OER activity of $Ni(OH)_2$/meso-Ir than Ni-B_i/meso-Ir (**Figure S12d**) is supported by previous research reporting that B can facilitate the OER reaction because it provides more defects due to amorphous structure and may facilitate the formation of intermediate oxide/hydroxide species, thus enhancing the OER activity of Ni-B_i/meso-Ir.[62,63]

Durability and stability are also key factors in evaluating the performance of electrocatalysts. After undergoing 1000 cycles of OER tests, the activity of Ni-B_i/meso-Ir shows negligible losses (**Figure S13a**). A chronopotentiometry measurement conducted at a constant current density of 10 mA cm^{-2} demonstrates that Ni-B_i/meso-Ir undergoes a negligible activity degradation over 20 h (**Figure S13b**), revealing its excellent long-term durability. The good structural stability of Ni-B_i/meso-Ir is also evidenced by the SEM images of the sample obtained after the OER durability test (**Figure S13c,d**).

To better understand the origin of the catalytic improvement in the Ni-B_i/meso-Ir heterostructure, XPS measurements after OER durability test were further performed to investigate the chemical states at the surface of the electrode. An increased content of Ir oxide species was observed by XPS result (Ir 4*f*) after OER (**Figure S14a**), where the resulted IrO_x species have been considered as favorable active sites for OER.[17,64] The increase in the high-valent Ni^{3+} state (**Figure S14b**) can originate from the emergence of NiOOH,[65] which is a well-known active catalyst for alkaline OER.[61] An increase in lattice oxygen (O1) is also observed after the OER, further confirming the growth of the oxide/hydroxide species on the surface of the Ni-B_i/meso-Ir (**Figure S14c**), and likely responsible for diminishing the signal of the other species. For OER, reasonably adjusting the adsorption energy of OER intermediates (*OOH, *OH, and *O) on the catalyst is crucial to reduce the OER overpotential.[17] Although both IrO_x and NiO_x can serve as active sites for OER, their function remains different. The NiO_x species is weakly bonded with O* and the rate

determining step (RDS) of NiO_x is determined by the transformation of *OH into *O.[66,67] As for metal Ir, the RDS is the formation of OOH* because the IrO_x species formed *in-situ* bind with O* too strongly.[68] In other words, the OH* and O* species tend to be adsorbed on NiO_x and IrO_x species, respectively.[25] Density functional theory (DFT) studies previously reported that the introduction of Ir species into NiFe-based sites dramatically decreased the Gibbs free energy of the rate-determining step (the formation of OOH*), leading to substantially accelerated OER kinetics, especially under alkaline conditions.[26] Similar results could also be found for other heterostructured electrocatalysts combining Ir with non-noble metals (*eg*. Ni, Co, Fe).[24,25,30] Therefore, based on the above experimental results and discussion, it can be concluded that the design of the Ni-B_i/meso-Ir heterostructure ensures i) a large area of contact rich in active sites, and ii) the synergy between *in-situ* formed IrO_x and NiO_x species at the heterointerface, both promoting the formation of OOH*, which finally desorbs to generate oxygen.

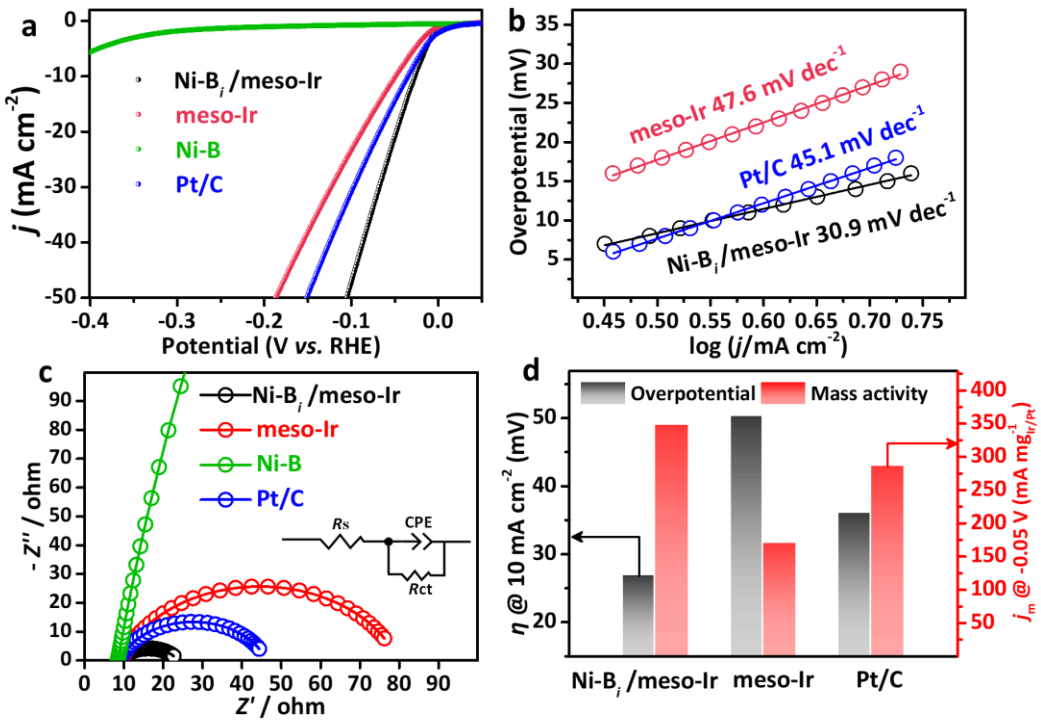

Figure 5. (a) HER polarization curves of Ni-B_i/meso-Ir, meso-Ir, Ni-B, and commercial Pt/C. (b) The corresponding Tafel plots of Ni-B_i/meso-Ir, meso-Ir, and commercial Pt/C. (c) EIS spectra (the inset shows the equivalent circuit model) of Ni-B_i/meso-Ir, meso-Ir and commercial Pt/C measured at −0.03 V *vs.* RHE in 1 M KOH. (d) η at 10 mA cm^{-2} and mass activity (j_m) at −0.05 V (*vs*. RHE) of Ni-B_i/meso-Ir, meso-Ir, and commercial Pt/C (the mass activities are normalized to loading amount of Ir or Pt on the electrode). All catalysts were examined using 1.0 M KOH as the electrolyte at the scan rate of 10 mV s^{-1} and corrected by *iR* compensation.

Besides OER, we also investigated the electrocatalytic activity of Ni-B_i/meso-Ir for HER under the same alkaline conditions (1.0 M KOH). As shown in **Figure 5a**, the Ni-B_i/meso-Ir heterostructured electrode exhibits the highest activity toward HER reaching to 10 mA cm^{-2} at an overpotential as low as 26.8 mV, lower than that of meso-Ir (50.2 mV) and commercial 20% Pt/C (36.0 mV). In addition, **Figure 5b** shows that Ni-B_i/meso-Ir possesses the least steep Tafel slope, in comparison with meso-Ir, and Pt/C, suggesting a faster HER reaction kinetics. The EIS results in **Figure 5c** show that Ni-B_i/meso-Ir heterostructures have the smallest R_{ct} compared with meso-Ir and Pt/C electrodes, suggesting a less resistive pathway to electron transfer under HER test conditions. Furthermore, the mass activity of Ni-B_i/meso-Ir is twice as large as that of meso-Ir, demonstrating a highly effective ECSA (**Figure 5d**). Because the performance of the Pt/C control is superior to the bare meso-Ir and Ni-B NPs, but inferior to the Ni-B_i/meso-Ir, the synergy between the Ir catalyst and amorphous Ni-B_i co-catalyst is clear. Unlike for OER, where both IrO_x and NiO_x species can work as active sites, the negligible HER activity of bare Ni-B NPs (**Figure 5a**) indicates that Ir is the main active species for HER while amorphous Ni-B_i layer acts as a co-catalyst in Ni-B_i/meso-Ir. In particular, because of the scarcely present H^+ in alkaline media, the process starts from the dissociation of H_2O molecules to supply protons.[69] Therefore, a subtle balance between the water dissociation (Volmer step) and the subsequent chemisorption of the water-splitting intermediates (OH^- and H*) is critical to promote HER performance.[70] In the current system, Ni^{x+} species can modify the electronic structure of Ir atoms, that is, the electron transfer from Ni-B_i to Ir (**Figure 2d-f**), which may weaken bonding strengths of hydrogen-containing intermediates, thus affecting the catalytic activity.[47] In addition, the hydrophilic Ni-based hydroxides layers may serve as H_2O anchoring sites to accelerate the sluggish water adsorption/dissociation processes.[71] As shown in **Figure S15**, the HER activity of $Ni(OH)_2$/meso-Ir is improved compared to bare meso-Ir, demonstrating the importance of hydrophilicity, but remains lower than that of Ni-B_i/meso-Ir. This highlights the importance of B in the electronic landscape of the heterostructure. Therefore, the improved HER activity can be directly imputed to combining Ir and Ni species, and to their interface. The Ni-B_i/meso-Ir electrode also exhibits excellent durability and long-term stability for HER (**Figure S16a,b**), also supported by its maintained structural integrity (**Figure S16c,d**). This contrasts with the bare meso-Ir, showing a significant decrease after 6 h stability test (**Figure S16b**), indicating that the presence of the Ni-B_i layer is crucial in improving stability.

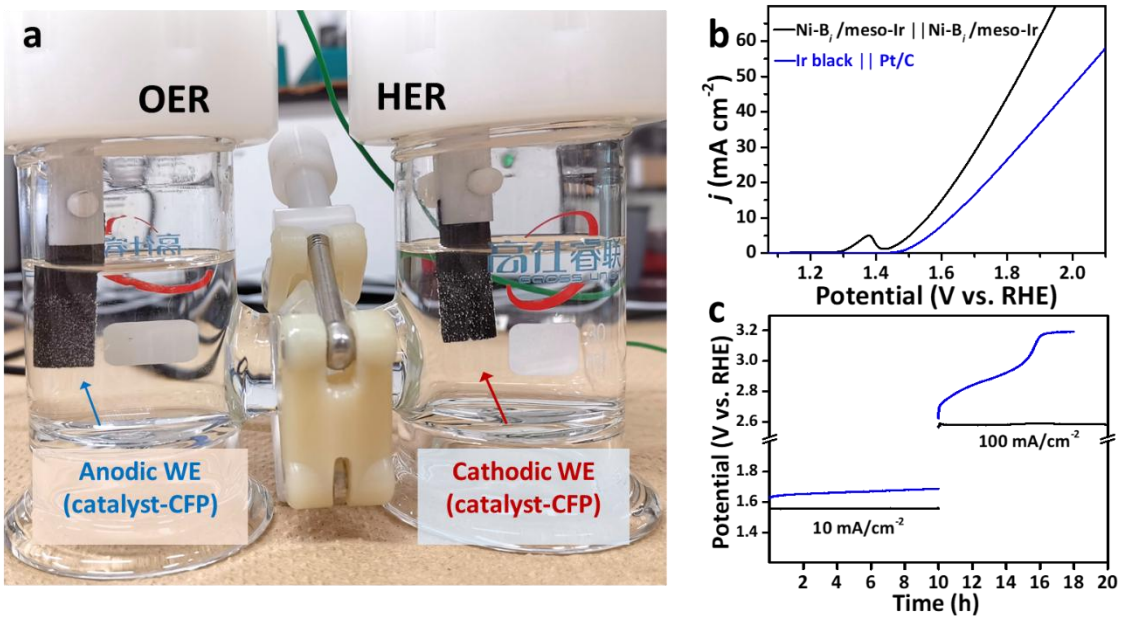

Figure 6. (a) Photograph of the electrochemical overall water splitting cell. (WE−working electrode, CFP−carbon fiber paper). (b) LSV curves of Ni-B$_i$/meso-Ir heterostructures and Ir black–Pt/C couple water electrolysis cell at a scan rate of 10 mV s^{-1} in 1.0 M KOH solution. (c) the corresponding chronopotentiometry curves of Ni-B$_i$/meso-Ir heterostructures and Ir black–Pt/C catalysts at 10 mA cm^{-2} and 100 mA cm^{-2}.

Encouraged by the excellent OER and HER performances, superior to those of most reported Ir-based catalysts (**Table S1**, **S2**), the dual-phase Ni-B$_i$/meso-Ir heterostructures are expected to serve as both anode and cathode for overall water splitting in a 1.0 M KOH solution. Therefore, we loaded the Ni-B$_i$/meso-Ir catalyst on carbon fiber paper (CFP) to construct a two–electrode water electrolysis cell and acquired their activities by LSV. As shown in **Figure 6a**, the H_2 and O_2 bubbles can be clearly seen from both the cathode and anode during the electrolysis process, respectively. The LSV curves in **Figure 6b** indicate that the cell with the Ni-B$_i$/meso-Ir requires only 1.55 V to reach a current density of 10 mA cm^{-2}, outperforming the coupled commercial benchmark Ir black || Pt/C catalysts. In addition, the Ni-B$_i$/meso-Ir-based device also exhibits higher catalytic stability than that using commercial catalysts at both low (10 mA cm^{-2}) and high (100 mA cm^{-2}) current density (**Figure 6c**). Furthermore, the faradaic efficiency for H_2 and O_2 generation by this electrolyzer was also evaluated by comparing the experimentally generated gas volume and theoretically calculated gas volume (**Figure S17**). The H_2:O_2 gas volume ratio close to 2:1 can be observed, with a faradaic efficiency of 98.1% and 97.4% for HER and OER, respectively. The prominent water splitting performance of dual-phase Ni-B$_i$/meso-Ir heterostructures could be ascribed to three reasons: (1) the well-defined 2D mesoporous nanosheets possess large specific surface area, rich active sites, and short

mass/charge transport distance; (2) the as-formed face-contact amorphous-crystalline heterointerfaces significantly synergistic interaction between meso-Ir and Ni-B_i layers, and facilitate the electron transfer between metals and boron; (3) the amorphous Ni-B_i layers ensure a sufficient adsorption sites of the catalyst and enhance the hydrophilicity.

Conclusion

In conclusion, we have presented a simple approach for developing highly efficient overall water splitting electrocatalyst by taking advantages of heterostructure engineering. The crystalline meso-Ir modified by amorphous nickel boron oxide layers forming a Ni-B_i/meso-Ir heterostructure exhibits outstanding OER and HER electrocatalytic activities and long-term durability in an alkaline media, superior to bare meso-Ir, Ni-B NPs and commercial state-of-the-art catalysts. The presence of Ni-B_i layers not only guarantees favorable electron transfer between meso-Ir and Ni-B_i but also improves the catalyst hydrophilicity to promote water adsorption, resulting in the enhanced catalytic performance. Meanwhile, the unique strong coupled 2D mesoporous heterostructure results in a large number of heterojunction interfaces and many active sites, as well as accelerate mass diffusion and electron transfer ability. Thus, our work highlights the importance of rational heterostructures interface engineering and provides a simple route to future design advanced electrocatalysts.

Acknowledgements

This work was supported by the China Scholarship Council (CSC). This work is supported by the JST-ERATO Yamauchi Materials Space-Tectonics Project (JPMJER2003). The authors are also grateful to the Queensland node of the Australian National Fabrication Facility (ANFF).

Conflict of interest

The authors declare no conflict of interest.

References

[1] J. Greeley, T. F.mJaramillo, J. Bonde, I. Chorkendorff, J. K. Nørskov, *Nat. Mater.* **2006**, *5*, 909.

[2] J. Kibsgaard, I. Chorkendorff, *Nat. Energy* **2019**, *4*, 430.

[3] F. Yu, H. Zhou, Y. Huang, J. Sun, F. Qin, J. Bao, W.A. Goddard III, S. Chen, Z. Ren, *Nat. Commun.* **2018**, *9*, 2551.

[4] C. Hu, L. Zhang, J. Gong, *Energy Environ. Sci.* **2019**, *12*, 2620.

[5] H. Li, S. Chen, Y. Zhang, Q. Zhang, X. Jia, Q. Zhang, L. Gu, X. Sun, L. Song, X. Wang, *Nat. Commun.*

2018, *9*, 2452.

[6] K. Tu, D. Tranca, F. Rodriguez-Hernandez, K. Jiang, S. Huang, Q. Zheng, M.-X. Chen, C. Lu, Y. Su, Z. Chen, H. Mao, C. Yang, J. Jiang, H.-W. Liang, X. Zhuang, *Adv. Mater.* **2020**, *32*, 2005433.

[7] T. A. Shifa, F. Wang, Y. Liu, J. He, *Adv. Mater.* **2019**, *31*, 1804828.

[8] Y. Liu, N. O. Weiss, X. Duan, H.-C. Cheng, Y. Huang, X. Duan, *Nat. Rev. Mater.* **2016**, *1*, 16042.

[9] Y. Jiang, H.-Y. Chen, J.-Y. Li, J.-F. Liao, H.-H. Zhang, X.-D. Wang, D.-B. Kuang, *Adv. Funct. Mater.* **2020**, *30*, 2004293.

[10] J. Diao, Y. Qiu, S. Liu, W. Wang, K. Chen, H. Li, W. Yuan, Y. Qu, X. Guo, *Adv. Mater.* **2020**, *32*, 1905679.

[11] F. Dong, T. Xiong, Y. Sun, Y. Zhang, Y. Zhou, *Chem. Commun.* **2015**, *51*, 8249.

[12] D. Zhang, H. Mou, F. Lu, C. Song, D. Wang, *Appl. Catal., B* **2019**, *254*, 471.

[13] A. Muthurasu, V. Maruthapandian, H. Y. Kim, *Appl. Catal., B* **2019**, *248*, 202.

[14] A. Wu, Y. Xie, H. Ma, C. Tian, Y. Gu, H. Yan, X. Zhang, G. Yang, H. Fu, *Nano Energy* **2018**, *44*, 353.

[15] A. Pandey, A. Mukherjee, S. Chakrabarty, D. Chanda, S. Basu, *ACS Appl. Mater. Interfaces* **2019**, *11*, 42094.

[16] Z. Zhuang, Y. Li, Z. Li, F. Lv, Z. Lang, K. Zhao, L. Zhou, L. Moskaleva, S. Guo, L. Mai, *Angew. Chem. Int. Ed.* **2018**, *57*, 496.

[17] Z. Chen, X. Duan, W. Wei, S. Wang, B.-J. Ni, *Nano Energy* **2020**, *78*, 105270.

[18] B. Jiang, J. Kim, Y. Guo, K. C. W. S. Wu, M. Alshehri, T. Ahamad, N. Alhokbany, J. Henzie, Y. Yamachi, *Catal. Sci. Technol.* **2019**, 9, 3697.

[19] Y. Pi, N. Zhang, S. Guo, J. Guo, X. Huang, *Nano Lett.* **2016**, *16*, 4424

[20] S.-H. Cho, K. R. Yoon, K. Shin, J.-W. Jung, C. Kim, J. Y. Cheong, D.-Y. Youn, S. W. Song, G. Henkelman, I-D. Kim, *Chem. Mater.* **2018**, *30*, 5941.

[21] B. M. Tackett, W. Sheng, S. Katte, S. Yao, B. Yan, K. A. Kuttiyiel, Q. Wu, J. G. Chen, *ACS Catal.* **2018**, *8*, 2615.

[22] Y. Xing, J. Ku, W. Fu, L. Wang, H. Chen, *Chem. Eng. J.* **2020**, *395*, 125149.

[23] W. Wang, S. Xi, Y. Shao, X. Gao, J. Lin, C. Meng, W. Wang, X. Guo, G. Li, *ChemElectroChem* **2019**, *6*, 1846.

[24] Y. Zhang, C. Wu, H. Jiang, Y. Lin, H. Liu, Q. He, S. Chen, T. Duan, L. Song, *Adv. Mater.* **2018**, *30*, 1707522.

[25] G. Zhao, P. Li, N. Cheng, S. X. Dou, W. Sun, *Adv. Mater.* **2020**, *32*, 2000872.

[26] K. Jiang, M. Luo, M. Peng, Y. Yu, Y.-R. Lu, T.-S. Chan, P. Liu, F. M. F. de Groot, Y. Tan, *Nat.*

Commun. **2020**, *11*, 2701.

[27] Q. Wang, C.-Q. Xu, W. Liu, S.-F. Hung, H. B. Yang, J. Gao, W. Cai, H. M. Chen, J. Li, B. Liu, *Nat. Commun.* **2020**, *11*, 4246.

[28] B. Jiang, Y. Guo, J. Kim, A. E. Whitten, K. Wood, K. Kani, A. E. Rowan, J. Henzie, Y. Yamauchi, *J. Am. Chem. Soc.* **2018**, *140*, 12434.

[29] H. Cheng, N. Yang, X. Liu, Q. Yun, M. H. Goh, B. Chen, X. Qi, Q. Lu, X. Chen, W. Liu, L. Gu, H. Zhang, *Natl. Sci. Rev.* **2019**, *6*, 955.

[30] X. Luo, X. Wei, H. Zhong, H. Wang, Y. Wu, Q. Wang, W. Gu, M. Gu, S. P. Beckman, C. Zhu, *ACS Appl. Mater. Interfaces* **2020**, *12*, 3539.

[31] H. Xu, B. Fei, G. Cai, Y. Ha, J. Liu, H. Jia, J. Zhang, M. Liu, R. Wu, *Adv. Energy Mater.* **2019**, *10*, 1902714.

[32] Y. Kang, J. Henzie, H. Gu, J. Na, A. Fatehmulla, B. S. A. Shamsan, A. M. Aldhafiri, W. A. Farooq, Y. Bando, T. Asahi, B. Jiang, H. Li, Y. Yamauchi, *Small* **2020**, 16, 1906707.

[33] Y. Pei, G. Zhou, N. Luan, B. Zong, M. Qiao, F. F. Tao, *Chem. Soc. Rev.* **2012**, *41*, 8140.

[34] D. He, L. Zhang, D. He, G. Zhou, Y. Lin, Z. Deng, X. Hong, Y. Wu, C. Chen, Y. Li, *Nat. Commun.* **2016**, *7*, 12362.

[35] S. Carenco, D. Portehault, C. Boissiere, N. Mezailles, C. Sanchez, *Chem. Rev.* **2013**, *113*, 7981.

[36] H. Han, H. Choi, S. Mhin, Y.-R. Hong, K. M. Kim, J. Kwon, G. Ali, K. Y. Chung, M. Je, H. N. Umh, D.-H. Lim, K. Davey, S.-Z. Qiao, U. Paik, T. Song, *Energy Environ. Sci.* **2019**, *12*, 2443.

[37] X. Yin, Y. Wang, T.-H. Chang, P. Zhang, J. Li, P. Xue, Y. Long, J. L. Shohet, P. M. Voyles, Z. Ma, X. Wang, *Adv. Mater.* **2020**, *32*, 2000801.

[38] M.-Q. Yang, J. Dan, S. J. Pennycook, X. Lu, H. Zhu, Q.-H. Xu, H. J. Fan, G. W. Ho, *Mater. Horiz.*, **2017**, *4*, 885.

[39] J. Hu, S. Li, Y. Li, J. Wang, Y. Du, Z. Li, X. Han, J. Sun, P. Xu, *J Mater. Chem. A* **2020**, *8*, 23323.

[40] C. Liang, P. Zou, A. Nairan, Y. Zhang, J. Liu, K. Liu, S. Hu, F. Kang, H. J. Fan, C. Yang, *Energy Environ. Sci.* **2020**, *13*, 86.

[41] K. Jiang, K. Xu, S. Zou, W-B. Cai, *J. Am. Chem. Soc.* **2014**, *136*, 4861.

[42] H. Lv, D. Xu, C. Kong, Z. Liang, H. Zheng, Z. Huang, B. Liu, *ACS Cent. Sci.* **2020**, *6*, 2347.

[43] H. Lv, L. Sun, D. Xu, B. Liu, *Sci. Bull.* **2020**, *65*, 1823.

[44] Y. Yamauchi, T. Momma, T. Yokoshima, K. Kuroda, T. Osaka, *J. Mater. Chem.* **2005**, *15*, 1987.

[45] Z. Zhu, J. Ma, L. Xu, L. Xu, H. Li, H. Li, *ACS Catal.* **2012**, 2, 211.

[46] A. P. Grosvenor, M. C. Biesinger, R. St.C. Smart, N. S. Mclntyre, *Surf. Sci.* **2006**, *600*, 1771.

[47] G. Liu, W. Wang, Y. Wu, N. Li, F. Zhao, Q. Zhao, J. Li, *Appl. Catal., B* **2020**, *260*, 118199.

[48] S. Liu, Z. Hu, Y. Wu, J. Zhang, Y. Zhang, B. Cui, C. Liu, S. Hu, N. Zhao, X. Han, A. Cao, Y. Chen, Y. Deng, W. Hu, *Adv. Mater.* **2020**, *32*, 2006034.

[49] Y. Wang, Y. Zhou, M. Han, Y. Xi, H. You, X. Hao, Z. Li, J. Zhou, D. Song, D. Wang, F. Gao, *Small* **2019**, *15*, 1805435.

[50] D. Liu, S. Lu, Y. Xue, Z. Guan, J. Fang, W. Zhu, Z. Zhuang, *Nano Energy* **2019**, *59*, 26.

[51] H. Li, G. Chen, H. Yang, X. Wang, J. Liang, P. Liu, M. Chen, N. Zheng, *Angew. Chem. Int. Ed.* **2013**, *52*, 8368.

[52] J. W. Hong, Y. Kim, D. H. Wi, S. Lee, S.-U. Lee, Y. W. Lee, S.-I. Choi, S. W. Han, *Angew. Chem. Int. Ed.* **2016**, *55*, 2753.

[53] G. J. Arteaga, J. A. Anderson, C. H. Rochester, *Catal. Letters* **1999**, *58*, 189–194.

[54] L. Q. Wang, M. Bellini, J. Filippi, M. Folliero, A. Lavacchi, M. Innocenti, A. Marchionni, H. A. Miller, F. Vizza, *Appl. Energy* **2016**, *175*, 479.

[55] L. Dai, Q. Qin, P. Wang, X. Zhao, C. Hu, P. Liu, R. Qin, M. Chen, D. Ou, C. Xu, S. Mo, B. Wu, G. Fu, P. Zhang, N. Zheng, *Sci. Adv.* **2017**, *3*, 1701069.

[56] L. S. Ferreira, M. S. Rodrigues, J. C. M. de Carvalho, A. Lodi, E. Finocchio, P. Perego, A. Converti, Single Metal Systems. *Chem. Eng. J.* **2011**, *173*, 326.

[57] R. Tabaraki, A. Nateghi, *Ecol. Eng.* **2014**, *71*, 197.

[58] M. W. Louie, A. T. Bell, *J. Am. Chem.* Soc. **2013**, *135*, 12329.

[59] F. Dionigi, Z. Zeng, I. Sinev, T. Merzdorf, S. Deshpande, M. B. Lopez, S. Kunze, I. Zegkinoglou, H. Sarodnik, D. Fan, A. Bergmann, J. Drnec, J. F. Araujo, M. Gliech, D. Teschner, J. Zhu, W.-X. Li, J. Greeley, B. R. Cuenya, P. Strasser. *Nat. Commun.* **2020**, *11*, 2522.

[60] S. Anantharaj, S. R. Ede, K. Karthick, S. S. Sankar, K. Sangeetha, P. E. Karthik, S. Kundu, *Energy Environ. Sci.* **2018**, *11*, 744.

[61] N.-T. Suen, S.-F. Hung, Q. Quan, N. Zhang, Y.-J. Xu, H. M. Chen, *Chem. Soc. Rev.* **2017**, *46*, 337.

[62] S. Gupta, M. K. Patel, A. Miotello, N. Patel, *Adv. Funct. Mater.* **2020**, *30*, 19106481.

[63] T. Haq, S. A. Mansour, A. Munir, Y. Haik, *Adv. Funct. Mater.* **2020**, *30*, 1910309.

[64] F. Luo, L. Guo, Y. Xie, J. Xu, K. Qu, Z. Yang, *Appl. Catal., B* **2020**, *279*, 119394.

[65] J. Chen, F. Zheng, S.-J. Zhang, A. Fisher, Y. Zhou, Z. Wang, Y. Li, B.-B. Xu, J.-T. Li, S.-G. Sun, *ACS Catal.* **2018**, *8*, 11342.

[66] W. T. Hong, M. Risch, K. A. Stoerzinger, A. Grimaud, J. Suntivich, Y. S.- Horn, *Energy Environ. Sci.*, **2015**, *8*, 1404.

[67] O. D.-Morales, I. L.-Yanez, M. T. M. Koper, F. C.-Vallejo, *ACS Catal.* **2015**, *5*, 5380.

[68] H. G. S. Casalongue, M. L. Ng, S. Kaya, D. Friebel, H. Ogasawara, A. Nilsson, *Angew. Chem., Int. Ed.* **2014**, *53*, 7169.

[69] G. Zhao, K. Rui, S.X. Dou, W. Sun, *Adv. Funct.* Mater. **2018**, *28*, 1803291.

[70] R. Subbaraman, D. Tripkovic, D. Strmcink, K.-C. Chang, M. Uchimura, A.P. Paulikas, V. Stamenkovic, N. M. Markovic, *Science* **2011**, *334*, 1256.

[71] N. Danilovic, R. Subbaraman, D. Strmcnik, K.- C. Chang, A. P. Paulikas, V. R. Stamenkovic, N. M. Markovic, *Angew. Chem. Int. Ed. Engl.* **2012**, *51*, 12495.